A Model-Based Image Reconstruction Algorithm With Simultaneous Beam Hardening Correction for X-Ray CT

Pengchong Jin, Charles A. Bouman, *Fellow, IEEE*, and Ken D. Sauer, *Member, IEEE*

***Abstract*—Beam hardening is a well-known effect in X-ray CT scanning that is caused by the interaction of a broad polychromatic source spectrum with energy-dependent material attenuation. If the scanned object only consists of a single material, the beam hardening effect can be corrected by sinogram precorrection techniques. However, when multiple materials are present, it becomes much more difficult to fully compensate for this distortion; in general, the beam hardening can contribute to reconstruction artifacts such as cupping and streaking. In this paper, we present a novel model-based iterative reconstruction algorithm that incorporates beam hardening correction (MBIR-BHC). Unlike most correction algorithms, which require knowledge of the X-ray spectrum or mass attenuation functions, the MBIR-BHC algorithm works by simultaneously reconstructing the image and estimating the beam-hardening function. The method is based on the assumption that the object is formed by a combination of two distinct materials that can be separated based on their densities. We formulate a poly-energetic X-ray forward model using a polynomial function of two material projections: one for the low-density material and one for the high. We then develop an alternating minimization algorithm for jointly estimating the reconstructed image, the material segmentation, and the coefficients of the two component polynomial that models the beam-hardening function. With this approach, the spectrum and mass attenuation functions are not needed in advance, and the correction is adapted to the dataset being reconstructed. We examine the performance of the proposed algorithm using both simulated and real datasets. Results indicate that the MBIR-BHC algorithm significantly reduces several reconstruction artifacts without advanced knowledge of the X-ray spectrum and material properties.**

***Index Terms*—X-ray CT, model-based iterative reconstruction (MBIR), beam hardening correction, poly-energetic.**

I. Introduction

X-RAY computed tomography (CT) is a widely used imaging modality that depends on the reconstruction of material cross-sections from line integrals of X-ray density. Typically, the required line integrals are obtained by assuming that the X-rays are attenuated exponentially as predicted by Beer-Lambert's law [1]. However, this approximation only holds when the X-ray source is monochromatic. When the X-ray source has a broad spectrum, low-energy photons are typically attenuated more rapidly than high-energy photons; so the beam shifts toward higher energies (i.e., is "hardened") as it passes through the material. The total attenuation is formed by the superposition of weighted exponentials, resulting in the so-called beam-hardening effect [2], [3]. In practice, beam hardening can contribute to cupping and streaking artifacts in the reconstructed images [2]–[7].

Various algorithms have been proposed to address the beam hardening effect [8]–[33]. One early approach was to pre-filter the X-ray beam [19] by placing a thin metal plate between the X-ray source and the objects, so as to pre-attenuate the low-energy photons. While such a method is able to narrow the X-ray spectrum and, therefore, reduce the beam hardening effect, it also lowers the detected signal to noise ratio (SNR). Another approach is dual energy scanning [11], [12]. These methods work by reconstructing two material-independent density maps from low and high-energy X-ray measurements. While this technique can fully account for beam-hardening, it requires two spectrally district projection measurements, which is generally much more complex and expensive.

Algorithmic correction is perhaps the most common approach to beam-hardening correction. One widely-used algorithmic correction is linearization, or polynomial pre-correction [2], [8]–[10]. Pre-correction techniques are based on the assumption that the object is made from a single material, such as water. However, when multiple materials are present, it is not possible to fully compensate for the beam hardening distortion using a single pre-correction function. Alternatively, iterative post-processing techniques are also widely used when the object being scanned is composed of two known materials that can be easily segmented [13]–[17]. These methods correct the sinogram using knowledge of the two materials' mass attenuation functions, the X-ray source spectrum, and an approximate spatial segmentation into the two materials. In medical imaging applications, it may be reasonable to assume that the object being scanned can be approximately segmented into two known materials, (e.g., soft issue and bone) and the X-ray spectrum is known; so these iterative post-processing techniques can be effective [13], [15], [16]. However, in more general CT applications, such as non-destructive evaluation

Manuscript received June 10, 2015; accepted June 11, 2015. Date of publication July 28, 2015; date of current version October 26, 2015. This work was supported in part by the U.S. Department of Homeland Security under Grant 2013-ST-061-ED000, and in part by the Showalter Trust Endowment. The views and conclusions contained in this document are those of the authors and should not be interpreted as necessarily representing the official policies, either expressed or implied, of the U.S. Department of Homeland Security. The associate editor coordinating the review of this manuscript and approving it for publication was Prof. W. Clem Karl.

P. Jin and C. A. Bouman are with the School of Electrical and Computer Engineering, Purdue University, West Lafayette, IN 47907-0501 USA (e-mail: jin36@purdue.edu; bouman@ecn.purdue.edu).

K. D. Sauer is with the Department of Electrical Engineering, University of Notre Dame, Notre Dame, IN 46556-5637 USA (e-mail: sauer@nd.edu).

Color versions of one or more of the figures in this paper are available online at http://ieeexplore.ieee.org.

Digital Object Identifier 10.1109/TCI.2015.2461492

or security scanning, the objects being scanned may be composed of a number of unknown materials. So the assumptions of iterative post-processing algorithms are violated, and the methods are not straightforward to apply.

Recent results in model-based iterative reconstruction (MBIR) have demonstrated its ability to improve the reconstructed image quality [34]–[39]. MBIR algorithms typically work by first formulating an overall objective function which incorporates statistical models of both the forward acquisition processes and the objects being reconstructed. The resulting objective functions are then minimized using iterative optimization methods. Several methods have also been developed in order to address the problem of beam hardening in the context of iterative reconstruction [22]–[25]. De Man *et al.* [22] proposed an iterative method which incorporated the knowledge of the known X-ray spectrum into the reconstruction process in order to account for the beam hardening effect. Elbakri *et al.* [23], [24] developed an iterative reconstruction method based on the idea of material decomposition. The joint beam hardening correction polynomial for a set of pre-determined basis materials is pre-calculated and tabulated, and is utilized during the iterative reconstruction. Srivastava *et al.* [26] and Abella *et al.* [30] extended Elbakri's approach. Their strategy is to design functionals with tuning parameters so that it can map the non-linear effect of two materials into one equivalent material. Therefore, only a single material beam hardening correction polynomial is required. However, all these methods require some additional knowledge of the system, such as X-ray spectrum and mass attenuation functions of the basis materials. In an alternative approach, Kyriakou *et al.* proposed a method called Empirical Beam Hardening Correction (EBHC), which does not rely on the prior knowledge of the X-ray spectrum or mass attenuation functions [31]. EBHC is based on direct reconstruction of a set of images formed from sinograms corresponding to the low and high-density components of the image. This set of reconstructions are combined in a way that maximizes flatness of the final corrected image.

In this paper, we propose a novel model-based iterative reconstruction algorithm including correction of beam hardening effects (MBIR-BHC). A preliminary study of this method was presented in conference paper [40]. Unlike most previous methods, which require additional system information in advance, MBIR-BHC works by simultaneously reconstructing the image and estimating the beam hardening correction function. The method is based on the assumption that the object is formed by a combination of two distinct materials that can be separated according to their densities. We formulate a poly-energetic X-ray forward model using a polynomial function of two material projections: one for the low density material and one for the high. We then develop an effective alternating optimization algorithm for estimating the reconstructed image, the material segmentation, and the coefficients of the two component polynomial. Since the correction polynomial and materials segmentation mask are both estimated during the reconstruction process, no additional system information is needed and the correction is automatically adapted to the dataset being reconstructed.

We evaluate the proposed MBIR-BHC algorithm using both simulated and real X-ray CT datasets, including high and low density objects. The experimental results show that the MBIR-BHC algorithm significantly reduces several reconstruction artifacts and improves the overall image quality.

The paper is organized as follows. Section II presents the poly-energetic X-ray model and formulates the problem of joint reconstruction and correction. Section III describes the alternating optimization. Section IV shows the experimental results on the simulated and real data to demonstrate the improvement achieved by MBIR-BHC as compared to traditional methods. Finally, Section V concludes the discussion.

II. Poly-energetic X-ray Model and Statistical Approach for Reconstruction

A. Poly-energetic Model for X-ray CT

Let $\mu(\mathcal{E}) \in \mathbb{R}^N$ be the vector whose the j-th entry $\mu_j(\mathcal{E})$ is the energy-dependent linear attenuation coefficient of the j-th pixel. The received photon intensity of the i-th projection, denoted by λ_i, can be modeled as a Poisson random variable with the mean given by

$$\mathbb{E}[\lambda_i|\mu(\mathcal{E})] = \int_{\mathbb{R}} S_i(\mathcal{E}) e^{-\sum_j A_{i,j}\mu_j(\mathcal{E})} d\mathcal{E} \tag{1}$$

where $S_i(\mathcal{E})$ is the source-detector energy spectrum, and A is the system forward projection matrix whose entries represent the contribution of the i-th projection to the j-th pixel. For each projection, the standard CT projection measurement Y_i is generated by

$$Y_i = -\log \frac{\lambda_i}{\lambda_{T,i}} \tag{2}$$

where $\lambda_{T,i}$ is the expected photon intensity in an air-calibration scan for the i-th projection, given by

$$\lambda_{T,i} = \int_{\mathbb{R}} S_i(\mathcal{E}) d\mathcal{E}. \tag{3}$$

Denote the normalized energy spectrum as $\tilde{S}_i$ given by

$$\tilde{S}_i(\mathcal{E}) = \frac{S_i(\mathcal{E})}{\lambda_{T,i}}. \tag{4}$$

We will assume that $\tilde{S}_i(\mathcal{E})$ is the same for all the projections; so the projection index i can be dropped in $\tilde{S}_i$. Putting (1) through (4), the expected projection measurement can be approximated as

$$\begin{aligned}\mathbb{E}[Y_i|\mu(\mathcal{E})] &\cong -\log\left(\mathbb{E}\left[\frac{\lambda_i}{\lambda_{T,i}}\right]\right)\\ &= -\log\left(\int_{\mathbb{R}} \tilde{S}(\mathcal{E}) e^{-\sum_j A_{i,j}\mu_j(\mathcal{E})} d\mathcal{E}\right).\end{aligned} \tag{5}$$

So (5) is the conventional model for the non-linear beam hardening that results from a poly-energetic X-ray beam.

Our objective will be to formulate a simple parametric model of the beam-hardening that occurs with a single, polychromatic scan of an object composed of two distinct materials, one with high density and the other with low. To do this, we first define x_j to be the weighted average of the linear attenuation coefficient of the j-th pixel with respect to the energy spectrum

$$x_j \triangleq \int_{\mathbb{R}} \tilde{S}(\mathcal{E})\mu_j(\mathcal{E})d\mathcal{E}. \tag{6}$$

Using this definition, we can rewrite the energy-dependent linear attenuation coefficient of the j-th pixel as

$$\mu_j(\mathcal{E}) = x_j r_j(\mathcal{E}) \tag{7}$$

where $r_j(\mathcal{E})$ is the absorption spectrum of the j-th pixel, given by

$$r_j(\mathcal{E}) = \frac{\mu_j(\mathcal{E})}{x_j} = \frac{\mu_j(\mathcal{E})}{\int_{\mathbb{R}} \tilde{S}(\mathcal{E})\mu_j(\mathcal{E})d\mathcal{E}}. \tag{8}$$

Notice that in this formulation, $r_j(\mathcal{E})$ carries the energy dependency and x_j only depends on the pixel location j. Moreover, from (8) we see that the weighted energy spectrum of $r_j(\mathcal{E})$ is normalized to 1; so for all j

$$\int_{\mathbb{R}} \tilde{S}(\mathcal{E})r_j(\mathcal{E})d\mathcal{E} = 1. \tag{9}$$

We first consider the simple case when the scanned object only contains one absorptive material denoted by $\mathcal{M}$. The functions $r_j(\mathcal{E})$ are identical for all pixels j and we have

$$\mu_j(\mathcal{E}) = x_j r_{\mathcal{M}}(\mathcal{E}) \tag{10}$$

where $r_{\mathcal{M}}(\mathcal{E})$ is the absorption spectrum for the material $\mathcal{M}$. Substituting (10) into (5), we may define the beam hardening function $f_{\mathcal{M}}(p_i)$ given by

$$f_{\mathcal{M}}(p_i) \triangleq -\log\left(\int_{\mathbb{R}} \tilde{S}(\mathcal{E})e^{-r_{\mathcal{M}}(\mathcal{E})p_i}d\mathcal{E}\right) \tag{11}$$

where p_i is the i-th projection given by

$$p_i = \sum_j A_{i,j}x_j. \tag{12}$$

Let $x \in \mathbb{R}^N$ be the vector with entries x_j defined in (6). Using this notation, the expected projection measurement is then given by

$$\mathbb{E}[Y_i|x] = f_{\mathcal{M}}(p_i). \tag{13}$$

So from (13), we see that the expected projection measurement $\mathbb{E}[Y_i|x]$ will be a non-linear function $f_{\mathcal{M}}$ of the projection p_i. Differentiating (11), we show in Appendix V that

$$\frac{d}{dp_i} f_{\mathcal{M}}(p_i)|_{p_i=0} = 1, \tag{14}$$

and therefore, we also know that

$$\frac{d}{dy_i} f_{\mathcal{M}}^{-1}(y_i)|_{y_i=0} = 1 \tag{15}$$

where y_i is the dummy variable for the inverse function $f_{\mathcal{M}}^{-1}$. This implies that when the value of the projection is very small (i.e. when the projection passes through a thin soft material), the beam hardening effect is negligible. In practice, since human soft tissue has energy-dependent attenuation similar to water, most current medical systems perform a beam hardening pre-correction with respect to water. More specifically, typical medical imaging systems apply a beam-hardening correction with the form $f_{\mathcal{M}}^{-1} = f_W^{-1}$, where the subscript W explicitly indicates water as the reference material.

Next consider the case of two materials. In this case, a single correction function can not fully compensate for the effects of beam hardening. In order to better model this case, we will assume the object is made of two distinct materials, one of low density and a second of high density. More formally, we model the absorption spectrum $r_j(\mathcal{E})$ as a convex combination of two distinct absorption spectra given by

$$r_j(\mathcal{E}) \triangleq (1-b_j)r_L(\mathcal{E}) + b_j r_H(\mathcal{E}), \tag{16}$$

where $r_L(\mathcal{E})$ and $r_H(\mathcal{E})$ represent the absorption spectrum of the "low" and "high" density materials respectively, and b_j represents the fraction of material that is of high density for the j-th pixel. Using this model, the linear attenuation coefficient of the j-th pixel can be written as

$$\mu_j(\mathcal{E}) = x_j\left((1-b_j)r_L(\mathcal{E}) + b_j r_H(\mathcal{E})\right). \tag{17}$$

In this work, we consider only the case in which b_j is binary, i.e. $b_j \in \{0, 1\}$; so each pixel will be composed entirely of either low or high density materials. In order to determine the values of b_j, we will estimate them directly from the CT data as part of the reconstruction process. While more discrete classes could be used, this simple two-material decomposition model strikes a balance between accuracy and model simplicity.

Substituting (17) into (5), we obtain

$$\mathbb{E}[Y_i|x] = h(p_{L,i}, p_{H,i}) \tag{18}$$

where $h(p_{L,i}, p_{H,i})$ is now a two dimensional beam hardening function given by

$$h(p_{L,i}, p_{H,i}) \triangleq -\log\left(\int_{\mathbb{R}} \tilde{S}(\mathcal{E})e^{-r_L(\mathcal{E})p_{L,i} - r_H(\mathcal{E})p_{H,i}}d\mathcal{E}\right) \tag{19}$$

and $p_{L,i}$ and $p_{H,i}$ are now the projections of the low and high density materials given by

$$p_{L,i} = \sum_j A_{i,j}x_j(1-b_j), \tag{20}$$

$$p_{H,i} = \sum_j A_{i,j}x_j b_j. \tag{21}$$

So from (18), we see that with two materials, the expected projection measurement is now a non-linear function of the two dimensional projections of the two materials. Our approach will be to adaptively estimate this 2D beam hardening function

TABLE I
COEFFICIENTS OF THE BEAM HARDENING FUNCTION h USED FOR UN-CORRECTED DATA

	$l=0$	$l=1$	$l=2$	$l=3$	$\cdots$
$k=0$	0	1	$\gamma_{0,2}$	$\gamma_{0,3}$	$\cdots$
$k=1$	1	$\gamma_{1,1}$	$\gamma_{1,2}$	$\gamma_{1,3}$	$\cdots$
$k=2$	$\gamma_{2,0}$	$\gamma_{2,1}$	$\gamma_{2,2}$	$\gamma_{2,3}$	$\cdots$
$k=3$	$\gamma_{3,0}$	$\vdots$	$\vdots$	$\vdots$	$\ddots$

TABLE II
COEFFICIENTS OF THE BEAM HARDENING FUNCTION $\tilde{h}$ USED FOR PRE-CORRECTED DATA

	$l=0$	$l=1$	$l=2$	$l=3$	$\cdots$
$k=0$	0	1	$\tilde{\gamma}_{0,2}$	$\tilde{\gamma}_{0,3}$	$\cdots$
$k=1$	1	$\tilde{\gamma}_{1,1}$	$\tilde{\gamma}_{1,2}$	$\tilde{\gamma}_{1,3}$	$\cdots$
$k=2$	0	$\tilde{\gamma}_{2,1}$	$\tilde{\gamma}_{2,2}$	$\tilde{\gamma}_{2,3}$	$\cdots$
$k=3$	0	$\vdots$	$\vdots$	$\vdots$	$\ddots$

during the reconstruction process. To do this, we adopt a simple polynomial parametrization of the function given by

$$h(p_{L,i}, p_{H,i}) = \sum_{k=0}^{\infty}\sum_{l=0}^{\infty} \gamma_{k,l}(p_{L,i})^k (p_{H,i})^l, \tag{22}$$

where $\gamma_{k,l}$ are coefficients to be jointly estimated during the reconstruction. Notice that the idea that using the polynomial to fit the multi-material beam hardening function has been used in various correction algorithms before [3], [23], [41].

In fact, some of the coefficients in (22) are determined by the physics; so this will simplify our problem. More specifically, if both the projections $p_{L,i}$ and $p_{H,i}$ are 0, plugging them into (19), we see that

$$\gamma_{0,0} = h(0,0) = -\log\left(\int_{\mathbb{R}} \tilde{S}(\mathcal{E})e^0 d\mathcal{E}\right) = 0. \tag{23}$$

Also differentiating (19) with respect to $p_{L,i}$ and $p_{H,i}$, we obtain in Appendix V the following two relationships

$$\gamma_{1,0} = \frac{\partial}{\partial p_{L,i}} h(p_{L,i}, 0)\,\big|_{p_{L,i}=0} = 1, \tag{24}$$

$$\gamma_{0,1} = \frac{\partial}{\partial p_{H,i}} h(0, p_{H,i})\,\big|_{p_{H,i}=0} = 1. \tag{25}$$

Table I lists the coefficients of the function h. We will refer to an p-th order model as one that includes all the unknown coefficients for $0 \le k + l \le p$.

This two-material beam-hardening model can also be used in the case when the projection measurement is pre-corrected for beam hardening of a single material. To see this, suppose the projection measurements have been pre-corrected with respect to the material $\mathcal{M}$ using the function $f_{\mathcal{M}}^{-1}$. As a result, the expected projection measurement, after pre-correction, is approximately given by

$$\mathbb{E}[Y_i|x] = \tilde{h}(p_{L,i}, p_{H,i}) \tag{26}$$

where the 2D beam hardening function $\tilde{h}$ is now given by

$$\tilde{h}(p_{L,i}, p_{H,i}) \triangleq f_{\mathcal{M}}^{-1} \cdot \left(-\log\left(\int_{\mathbb{R}} \tilde{S}(\mathcal{E})e^{-r_L(\mathcal{E})p_{L,i} - r_H(\mathcal{E})p_{H,i}} d\mathcal{E}\right)\right). \tag{27}$$

Using the similar approach as in (22), we can parametrize $\tilde{h}$ using a high-order polynomial as

$$\tilde{h}(p_{L,i}, p_{H,i}) = \sum_{k=0}^{\infty}\sum_{l=0}^{\infty} \tilde{\gamma}_{k,l}(p_{L,i})^k (p_{H,i})^l \tag{28}$$

where $\tilde{\gamma}_{k,l}$ are the polynomial coefficients. Moreover, we show in Appendix V that in this case similar constraints hold with

$$\tilde{\gamma}_{0,0} = \tilde{h}(0,0) = 0, \tag{29}$$

$$\tilde{\gamma}_{1,0} = \frac{\partial}{\partial p_{L,i}} \tilde{h}(p_{L,i}, 0)|_{p_{L,i}=0} = 1, \tag{30}$$

$$\tilde{\gamma}_{0,1} = \frac{\partial}{\partial p_{H,i}} \tilde{h}(0, p_{H,i})|_{p_{H,i}=0} = 1. \tag{31}$$

In practice, it is common to pre-correct the projection measurements, Y_i, for the beam hardening due to the low-density material. In medical applications, this correction is usually based on a water phantom since human soft tissue is largely composed of water. In this case, the pre-correction is given by $f_{\mathcal{M}}^{-1} = f_L^{-1}$ where f_L^{-1} is the ideal beam-hardening correction for the low density material. By definition, we know that this pre-correction will linearize the low density measurement so that

$$\tilde{h}(p_{L,i}, 0) = f_L^{-1}(f_L(p_{L,i})) = p_{L,i}. \tag{32}$$

This implies that $\tilde{\gamma}_{k,0} = 0$ for $k \neq 1$. Table II lists the coefficients of the function $\tilde{h}$.

In summary, we have shown that the two-material beam-hardening model can be used for both pre-corrected and un-corrected projection data. In both cases, the three coefficients $\gamma_{0,0} = 0$ and $\gamma_{0,1} = \gamma_{1,0} = 1$ are pre-determined. Depending on the selected model order, the set of remaining coefficients are then estimated as part of the reconstruction algorithm. In particular, for a 2-nd order model ($p = 2$), the unknown coefficients to be estimated are $\gamma_{k,l}$ for $(k,l) \in \{(1,1),(0,2)\}$; and for a 3-rd order model ($p = 3$), then the unknown coefficients to be estimated are $\gamma_{k,l}$ for $(k,l) \in \{(1,1),(2,1),(0,2),(1,2),(0,3)\}$.

As a final remark, we will use the unified notation $h(\cdot,\cdot)$ and $\gamma_{k,l}$ to denote the correction polynomial and its coefficients throughout the following discussion This is only to keep our notation simple. We will explicitly state the pre-correction information and the polynomial order we use when we present the experiment results.

B. Statistical Model and Objective Function

Let $x \in \mathbb{R}^N$ be the image vector, $y \in \mathbb{R}^M$ be the vector of the projection measurements, $b \in \{0,1\}^N$ be the vector of the material segmentation label mask, and $\gamma \in \mathbb{R}^K$ be the vector of the fitting coefficients $\gamma_{k,l}$. So $K = 2$ if the 2-nd order model in Table II is used and $K = 5$ if the 3-rd order model is used, etc.

We treat γ as the nuisance parameter and formulate the problem of simultaneous image reconstruction and beam hardening correction as the computation of the maximum a posterior (MAP) estimate given by

$$\{\hat{x}, \hat{b}, \hat{\gamma}\} = \arg\min_{x \geq 0, b, \gamma} \{-\log \mathbb{P}(y|x, b, \gamma) - \log \mathbb{P}(x, b)\} \tag{33}$$

where $\mathbb{P}(y|x, b, \gamma)$ is the likelihood function corresponding to the X-ray forward model, and $\mathbb{P}(x, b)$ is the joint prior distribution over the image x and the material segmentation mask b. Note that we require the image to be non-negative. The parameter vector γ is adaptively estimated in this framework. Such an approach has been studied previously in [42] and one may interpret it as computation of the joint maximum *a posteriori* (MAP) and maximum likelihood (ML) estimates of the unknown variables and the nuisance parameters, respectively.

Assuming the projection measurements Y_i are conditionally independent with mean given by (19), the negative log likelihood function can be written, within a constant, as

$$-\log \mathbb{P}(y|x, b, \gamma) \approx \frac{1}{2} \sum_{i=1}^{M} w_i (y_i - h(p_i))^2 \tag{34}$$

where γ is implicitly specified in $h(p_i)$ by (22) and $p_i = [p_{L,i}\ p_{H,i}]^T$, and w_i is the statistical weight for the i-th projection, which is approximately proportional to the inverse of variance of the measurement Y_i. Note that taking the log of the signal in equation (19) can cause a slight mean shift in the signal since the log is concave. However, for the purposes of this paper, we will assume that means shift is negligible. Using this assumption, w_i can also be computed approximately as

$$w_i = \frac{\lambda_i^2}{\lambda_i + \sigma_e^2} \tag{35}$$

where σ_e^2 is the variance of the additive electronic noise.

To model the joint prior over x and b, we adopt the Markov random field (MRF) model. We want to model not only the interactions among pixels or segmentation labels themselves, but also the interactions between pixels and segmentation labels. Our model is a two-layer pairwise MRF, one for the image x and the other for the material segmentation mask b. Nodes on one layer connect to their corresponding counterparts on the other. Note that the joint MRF model for image and segmentation label has also been applied in CT artifact reduction and segmentation problem [43]. Fig. 1 illustrates this graphical model. From this structure, we may write the joint prior distribution over x and b as

$$\mathbb{P}(x, b) = \frac{1}{Z} \exp \left\{ -\sum_{\{j,k\} \in \mathcal{C}} \alpha_{j,k} \rho(x_j, x_k) - \beta \sum_{j=1}^{N} \psi(x_j, b_j) - \sum_{\{j,k\} \in \mathcal{C}} \eta_{j,k} \phi(b_j, b_k) \right\} \tag{36}$$

where $\mathcal{C}$ denotes the set of all pairwise cliques, ρ, ψ and ϕ are the positive potential functions on x, b, and the interactions between them, respectively, and Z denotes the partition function making the whole function a valid probability distribution [44]. The parameters $\alpha_{j,k}$, β and $\eta_{j,k}$ are the corresponding weights for edges in the graph. We choose $\alpha_{j,k}$ and $\eta_{j,k}$ to be inversely proportional to the distance between pixel j and k. Moreover, the scales of these parameters are empirically adjusted to balance among noise, resolution and segmentation error in the final reconstruction. We have listed the selected parameters for each dataset we test in the Result section.

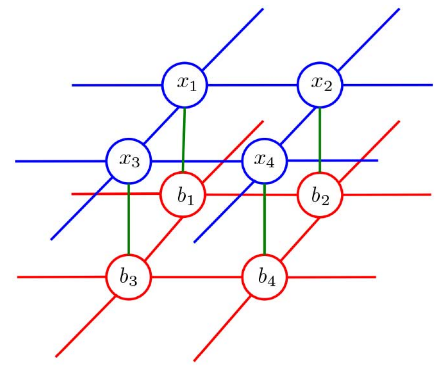

Fig. 1. Illustration of the joint prior over x and b as a two-layer MRF. Pixels x_j are connected through the blue potentials ρ. Material segmentation labels b_j are connected through the red potentials ϕ. Pixels and segmentation labels are also connected through the green potentials ψ.

For the pixel pairwise potential ρ, we use the q-generalized Gaussian MRF (q-GGMRF) potential function [35], given by

$$\rho(x_j, x_k) \triangleq \frac{|x_j - x_k|^p}{1 + |(x_j - x_k)/c|^{p-q}} \tag{37}$$

where $1 \leq q \leq p = 2$. Notice that the function only depends on the pixel difference $\Delta = x_j - x_k$ and a pair of pixels with small difference results high probability. Here c is a tuning parameter to balance the performance between noise reduction and edge preservation. If $|\Delta| \ll c$, $\rho(\Delta) \approx |\Delta|^p$ and if $|\Delta| \gg c$, $\rho(\Delta) \approx |\Delta/c|^q$.

The potential ψ, which captures the inter-layer interactions, should be chosen such that it gives high probabilities if the segmentation label correctly reflects the pixel value and gives low probabilities otherwise. We design the potential ψ to be

$$\psi(x_j, b_j) \triangleq (x_j - T)_+(1 - b_j) + (T - x_j)_+ b_j \tag{38}$$

where $(x)_+ = \max\{x, 0\}$ and T is the user-defined threshold. This is a linear loss function which penalizes the mismatch of the pixel and its corresponding segmentation label. Specifically, when $b_j = 0$, indicating that the pixel belongs to the low density material, ψ will impose a linear penalty if x_j exceeds the attenuation threshold T. Symmetrically, a linear penalty will be imposed in the case when $x_j \leq T$ and $b_j = 1$.

The potential ϕ over the binary segmentation label should encourage the similarity of the neighboring labels. We design it to be

$$\phi(b_j, b_k) \triangleq 1 - \delta(b_j - b_k) \tag{39}$$

where $\delta(\cdot)$ is the discrete delta function taking the value 1 at 0 and 0 elsewhere.

Combining the log likelihood term of (34) and the two-layer MRF joint prior over x and b in (36), we obtain the overall MAP estimation problem as

$$\{\hat{x}, \hat{b}, \hat{\gamma}\} = \arg\min_{x\geq 0, b, \gamma} \left\{ \frac{1}{2}\sum_{i=1}^{M} w_i (y_i - h(p_i))^2 + \sum_{\{j,k\}\in\mathcal{C}} \alpha_{j,k}\rho(x_j - x_k) + \sum_{\{j,k\}\in\mathcal{C}} \eta_{j,k}(1-\delta(b_j - b_k)) + \beta \sum_{j=1}^{N} ((x_j - T)_+(1-b_j) + (T-x_j)_+ b_j) \right\}. \quad (40)$$

We refer to (40) as the objective function in our reconstruction framework.

III. Iterative Beam Hardening Correction and Image Reconstruction

A. Estimation of the Beam Hardening Correction Polynomial

Fixing x and b, we first attack the problem of minimizing the objective function with respect to γ. This becomes a standard weighted least squares problem given by

$$\hat{\gamma} = \arg\min_{\gamma} \frac{1}{2}\sum_{i=1}^{M} w_i (y_i - h(p_i))^2 = \arg\min_{\gamma} \frac{1}{2}\|y - H\gamma\|_W^2 \quad (41)$$

where $H \in \mathbb{R}^{M\times K}$ is a matrix whose columns correspond specific terms in the correction polynomials of all the projections in (28) and $W = \mathrm{diag}\{w_1, \cdots, w_M\}$. The solution can then be computed in the closed form as

$$\hat{\gamma} = (H^T W H)^{-1} H^T W y. \quad (42)$$

B. Image Reconstruction as Optimization

Next, we fix γ and b and minimize the objective function (40) with respect to x. Since $h(p_i)$ is a polynomial function of p_i, which is in turn a linear function of x, (40) will be a higher order function of x, rather than a simple quadratic. Thus, the function (40) can be in general difficult to solve.

We approach the optimization by applying the Newton-Raphson technique. More specifically, we replace the original optimization (40) over x with the following modified optimization

$$\hat{x} = \arg\min_{x\geq 0} \left\{ \sum_{i=1}^{M} (d^{(i),T}(p_i - \hat{p}_i) + \frac{1}{2}(p_i - \hat{p}_i)^T Q^{(i)} (p_i - \hat{p}_i)) + \beta \sum_{j} ((x_j - T)_+(1-b_j) + (T-x_j)_+ b_j) + \sum_{\{j,k\}\in\mathcal{C}} \alpha_{j,k}\rho(x_j - x_k) \right\} \quad (43)$$

where $d^{(i)} \in \mathbb{R}^2$ and $Q^{(i)} \in \mathbb{R}^{2\times 2}$ are the gradient and Hessian of the function $\frac{1}{2}w_i(y_i - h(p_i))^2$ at the point $\hat{p}_i$, given by

$$d^{(i)} = -w_i(y_i - h(\hat{p}_i))\nabla h(\hat{p}_i), \quad (44)$$

$$Q^{(i)} = w_i \nabla h(\hat{p}_i)\nabla h(\hat{p}_i)^T - w_i(y_i - h(\hat{p}_i)\mathrm{Hess}(h(\hat{p}_i)), \quad (45)$$

and $\hat{p}_i$ is the projection vector of the previous estimate of $\hat{x}$. The term $\mathrm{Hess}(h(\hat{p}_i)) \in \mathbb{R}^{2\times 2}$ is given by

$$\mathrm{Hess}(h(\hat{p}_i)) = \begin{bmatrix} \frac{\partial^2}{\partial p_{L,i}^2} h(p_i) & \frac{\partial^2}{\partial p_{L,i}\partial p_{H,i}} h(p_i) \\ \frac{\partial^2}{\partial p_{L,i}\partial p_{H,i}} h(p_i) & \frac{\partial^2}{\partial p_{H,i}^2} h(p_i) \end{bmatrix} \Big|_{p_i = \hat{p}_i}. \quad (46)$$

By doing this, we essentially reduce (40) to (43), which is a quadratic function plus the remaining prior terms. The same approach has been used in other non-quadratic optimization problems such as [45], [46]. Such a quadratic approximation is generally not an upper bound, which means convergence of the algorithm is not guaranteed without further innovations. However, this approximation is effective and in practice, as we will show in the Results section, we have empirically observed that the resulting updates consistently reduce the objective function of (40). The overall algorithm works by first constructing the quadratic approximation (43) using the previous projections $\hat{p}_i$ and optimizing (43) to obtain the next estimate of $\hat{x}$. The projections $\hat{p}_i$ are then updated and are used in the next iteration.

There are a number of techniques that can be applied to optimize the quadratic approximation (43). We choose the iterative coordinate descent (ICD) algorithm. The ICD algorithm updates each pixel in sequence with the other pixels fixed until convergence. Here we present a sketch of derivations of the pixel update and more detailed derivations can be found in Appendix VI. Following the similar strategy in [36], the j-th pixel update can be computed by solving the 1D optimization given by

$$x_j = \arg\min_{u\geq 0} \left\{ \theta_1(u - \tilde{x}_j) + \frac{1}{2}\theta_2(u - \tilde{x}_j)^2 + \beta\left((u-T)_+(1-b_j) + (T-u)_+ b_j\right) + \sum_{k\in\partial j} \alpha'_{j,k}(u - x_k)^2 \right\} \quad (47)$$

where $\tilde{x}_j$ denotes the previous value of the pixel, ∂j represents the set of neighbors of the j-th pixel, and the coefficient ${\alpha'}_{j,k}$ is given by

$${\alpha'}_{j,k} = \alpha_{j,k}\frac{\rho'(\tilde{x}_j - x_k)}{2(\tilde{x}_j - x_k)}. \quad (48)$$

Here $\rho'(\cdot)$ is the first derivative of $\rho(\cdot)$ and θ_1 and θ_2 are the first and second derivatives of the first term in (43) with respect to x_j, given by

```
ICDUpdate { /* ICD update for the j-th pixel */
x̃_j ← x_j
θ_1, θ_2 ← calculate using (49) and (50)
D_1, D_2 ← calculate using (51) and (52)
if b_j = 0 then
  x_j ← calculate using (53)
  for i = 1 to M do
    p_{L,i} ← p_{L,i} + A_{i,j}(x_j − x̃_j)
  end for
else if b_j = 1 then
  x_j ← calculate using (55)
  for i = 1 to M do
    p_{H,i} ← p_{H,i} + A_{i,j}(x_j − x̃_j)
  end for
end if
return x_j
}
```

Fig. 2. Pseudocode of ICD update of the pixel x_j. First, we calculate the parameters θ_1, θ_2, D_1 and D_2. Second, we perform the update procedure according to (53) or (55) depending on the value of b_j. Finally, we update the projection vector using (56) and return the pixel update.

```
x ← from FBP or generic MBIR
b ← initially segment x using (57)
for i = 1 to M do
  p_i ← calculate using (20) and (21)
  p̂_i ← p_i
end for
repeat
  γ ← solution of (41)
  for i = 1 to M do
    d^(i), Q^(i) ← calculate using (44) and (45)
  end for
  for j = 1 to N do
    x_j ← calculate using ICDUpdate in Figure 2
  end for
  for j = 1 to N do
    b_j ← solution of (58)
    p_i ← updated using (59)
  end for
  for i = 1 to M do
    p̂_i ← p_i
  end for
until convergence
```

Fig. 3. Pseudocode of the MBIR-BHC algorithm for simultaneous image reconstruction and beam hardening correction. First, we initialize the reconstruction x and the segmentation b, and compute $\hat{p}_i$ for all i. Then, the algorithm iterates and for each iteration, the optimal coefficient $\hat{\gamma}$ is first calculated followed by the calculation of the parameters $d^{(i)}$ and $Q^{(i)}$ for all i. After that, the optimal x is solved by minimizing the quadratic approximation (43) and the optimal segmentation b is estimated using ICM. Finally, the expansion point is updated which will be used in the next iteration.

TABLE III
REGULARIZATION PARAMETER SETTING OF MBIR-BHC FOR DIFFERENT EXPERIMENTS

Experiment	α	β	η
two-material phantom	0.382	0.024	0.024
multi-material phantom (noiseless)	0.514	0.033	0.033
multi-material phantom (noisy)	0.013	0.033	0.033
modified NCAT phantom	0.630	0.040	0.040
real baggage scan	0.607	0.039	0.039

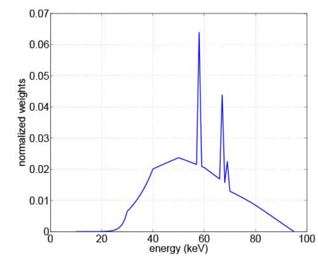

Fig. 4. Normalized energy spectrum of the X-ray source used for simulation.

$$\theta_1 = \sum_{i=1}^{M} \left(\left(d^{(i),T} + (p_i - \hat{p}_i)^T Q^{(i)} \right) \begin{bmatrix} A_{i,j}(1-b_j) \\ A_{i,j}b_j \end{bmatrix} \right) \tag{49}$$

$$\theta_2 = \sum_{i=1}^{M} \begin{bmatrix} A_{i,j}(1-b_j) \; A_{i,j}b_j \end{bmatrix} Q^{(i)} \begin{bmatrix} A_{i,j}(1-b_j) \\ A_{i,j}b_j \end{bmatrix}. \tag{50}$$

To obtain the optimal solution to (47), we define two quantities D_1 and D_2 as

$$D_1 = \theta_1 - \theta_2 \tilde{x}_j - 2 \sum_{k \in \partial j} \alpha'_{j,k} x_k, \tag{51}$$

$$D_2 = \theta_2 + 2 \sum_{k \in \partial j} \alpha'_{j,k}. \tag{52}$$

Using this notation, the optimal update can be obtained by applying a shrinkage operation. More specifically, when $b_j = 0$, we have the update given by

$$x_j \leftarrow \mathcal{S}_{\frac{\beta}{2D_2}} \left(-\frac{D_1}{D_2} - T - \frac{\beta}{2D_2} \right) + T \tag{53}$$

where the shrinkage operator is defined as

$$\mathcal{S}_\lambda(z) = \mathrm{sign}(z) \max\{|z| - \lambda, 0\}, \tag{54}$$

and when $b_j = 1$, we have

$$x_j \leftarrow \mathcal{S}_{\frac{\beta}{2D_2}} \left(-\frac{D_1}{D_2} - T + \frac{\beta}{2D_2} \right) + T. \tag{55}$$

Having obtained the optimal x_j, we then re-allocate the projection using the projection update equation given by

$$\begin{bmatrix} p_{L,i} \\ p_{H,i} \end{bmatrix} \leftarrow \begin{bmatrix} p_{L,i} \\ p_{H,i} \end{bmatrix} + \begin{bmatrix} A_{i,j}(1-b_j) \\ A_{i,j}b_j \end{bmatrix} (x_j - \tilde{x}_j). \tag{56}$$

This will finish the ICD update of one specific pixel. Fig. 2 summarizes the pseudocode of the ICD update for a specific pixel.

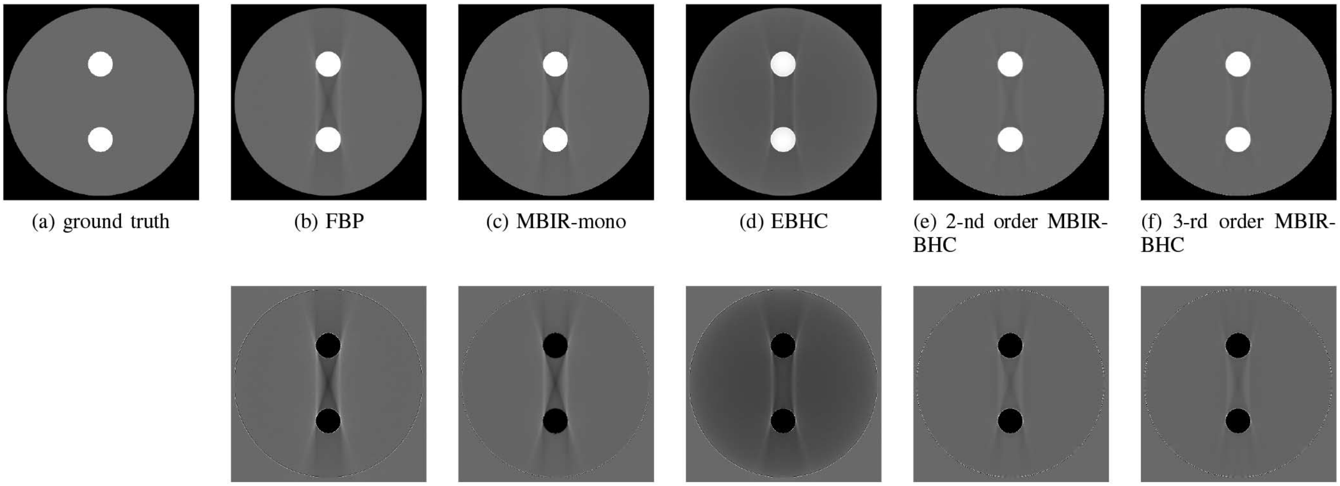

(a) ground truth (b) FBP (c) MBIR-mono (d) EBHC (e) 2-nd order MBIR-BHC (f) 3-rd order MBIR-BHC

(g) (b) - (a) (h) (c) - (a) (i) (d) - (a) (j) (e) - (a) (k) (f) - (a)

Fig. 5. Comparison of FBP, MBIR-mono, EBHC and 2-nd and 3-rd order MBIR-BHC reconstructed images. Top row: the reconstructed images. Bottom row: the difference images. The display window for the reconstructed images is [-400 400] HU. The display window for the difference images is [-200 200] HU. Notice that the MBIR-BHC algorithm reduces visible beam-hardening artifacts in the reconstruction of simulated data.

C. Optimization Over the Material Segmentation Mask

The segmentation vector b is initialized by thresholding the initial reconstruction $x^{(\text{init})}$ at the begining of the algorithm, given by

$$b_j = \begin{cases} 0, & \text{if } x_j^{(\text{init})} \le T \\ 1, & \text{otherwise.} \end{cases} \tag{57}$$

During the alternating optimization, we fix x and γ, and find the configuration of b which minimizes the overall objective function (40). We use the iterative conditional mode (ICM) algorithm. This requires us to solve the 1D optimization of a particular segmentation label as follows

$$\begin{aligned} b_j = \arg\min_{t \in \{0,1\}} \Bigg\{ & \frac{1}{2} \sum_{i=1}^{M} w_i (y_i - h(p_i))^2 \\ & + \sum_{k \in \partial j} \eta_{j,k} (1 - \delta(t - b_k)) \\ & + \beta((x_j - T)_+ (1 - t) + (T - x_j)_+ t) \Bigg\}. \end{aligned} \tag{58}$$

The actual implementation is to evaluate the 1D objective function (58) for $t = 0$ or 1 and to choose the optimal configuration of t which gives the lower cost. After the label is updated, we adjust the projection according to this optimal configuration. If we let $\tilde{b}_j$ and b_j be the labels of the pixel before and after the ICM update, the projection update is given by

$$\begin{bmatrix} p_{L,i} \\ p_{H,i} \end{bmatrix} \leftarrow \begin{bmatrix} p_{L,i} \\ p_{H,i} \end{bmatrix} + \begin{bmatrix} \tilde{b}_j - b_j \\ b_j - \tilde{b}_j \end{bmatrix} A_{i,j} x_j. \tag{59}$$

Fig. 3 shows the pseudocode of the overall MBIR-BHC algorithm for simultaneous image reconstruction and beam hardening correction, which alternates over the optimization of the polynomial coefficients γ, the image x and the material segmentation label mask b.

IV. Results

In the following section, we evaluate MBIR with beam-hardening correction (MBIR-BHC) using both simulated and real data sets, and we compare it to FBP, generic MBIR with a mono-energetic X-ray model (MBIR-mono), and the Empirical Beam Hardening Correction (EBHC) method [31]. The cost function for MBIR-mono is given by

$$\hat{x} = \arg\min_{x \ge 0} \left\{ \frac{1}{2} \|y - Ax\|_W^2 + \sum_{\{j,k\} \in \mathcal{C}} \alpha_{j,k} \rho(x_j - x_k) \right\}; \tag{60}$$

and we use the q-GGMRF potential function (37) for ρ. Both MBIR-mono and MBIR-BHC use the FBP reconstruction as an initial condition for optimization. Also, the segmentation, b_j, is initialized with a thresholded version of the FBP image, and we use a 3×3 neighborhood with coefficients $\alpha_{j,k}$ and $\eta_{j,k}$ selected so that

$$\alpha_{j,k} = \alpha g_{j,k}, \quad \eta_{j,k} = \eta g_{j,k}. \tag{61}$$

Here α, η are two scalars and $g_{j,k}$ are the relative weights for different neighboring pixels, given by the following 2D array of values,

0.11	0.14	0.11
0.14	0	0.14
0.11	0.14	0.11

where the center cell represents the pixel being considered. In Table III, we list the parameters α, β and η that were used for each experiment. For the EBHC method, the basic images are reconstructed using FBP. Unless otherwise stated, all MBIR-BHC results use a 2-nd order model with $p = 2$.

TABLE IV
MEAN INTENSITY (HU) OF THE WATER REGION IN FIG. 5

ground truth	0
FBP	-5.8
MBIR-mono	-7.5
EBHC	-44.2
2-nd order MBIR-BHC	-7.2
3-rd order MBIR-BHC	-7.3

A. Simulation Results

In this section, we study the performance of different methods on various phantoms using the computer-simulated parallel-beam transmission polychromatic X-ray projections. The X-ray source spectrum we use is modelled using SPEC78 software from IPEM Report 78 [47] (tube voltage 95 kV, incident mean 56.4093 keV, std 14.2177 keV), and its normalized energy spectrum is plotted in Fig. 4. Furthermore, in all the following simulation studies, the projections are pre-corrected with respect to water using the standard polynomial fitting technique described in [3]. The resulting pre-corrected projection will be used as the input for the different methods.

1) The Two-Material Disk Phantom: The first phantom we study is a two-material phantom, made of a water disk with two aluminium insertions, as shown in Fig. 5(a). The radius of the water disk and the aluminium insertions are 90 mm and 10 mm, respectively. The parallel-beam projection sinogram has 1024 detectors with 0.24 mm spacing and 720 projection angles over 180 degrees. We do not simulate the noise and scatter effects. All the reconstructed images are 512×512 over the 250 mm FOV. For MBIR-BHC, both the 2-nd and 3-rd order polynomial model are used and the segmentation threshold T is 800 HU. The reconstruction results using different methods are presented in Fig. 5(b)–(i). Both FBP and MBIR-mono reconstructions contain streak artifacts due to the aluminium insertions. The EBHC method is able to partially suppress the streaks. However, the dark band connecting two insertions is still noticeable. The MBIR-BHC reduces the streak artifacts more effectively. However, in this case, the 3-rd order MBIR-BHC model seems to provide little benefit relative to the 2-nd order MBIR-BHC model. In Table IV, the mean intensity of the water region is listed. Notice that the EBHC tends to introduce a bias in the reconstruction.

Using the two-material phantom, we further investigate the modeling error in MBIR-mono and MBIR-BHC method. In particular, we simulate the projection y_i as in (27) using Monte Carlo method followed by the water pre-correction, and calculate the modeling error as the difference between y_i and the forward projection of the phantom. Mathematically, the modeling error in MBIR-mono is given by

$$e_i^{(\text{MBIR-mono})} = y_i - \sum_{j=1}^{N} A_{i,j} x_j^{(\text{phantom})}, \tag{62}$$

and for MBIR-BHC, it is

$$e_i^{(\text{MBIR-BHC})} = y_i - \sum_{0 \le k+l \le p} \tilde{\gamma}_{k,l} (p_{L,i})^k (p_{H,i})^l \tag{63}$$

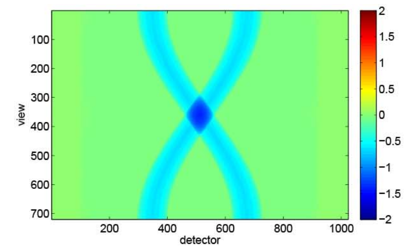

(a) MBIR-mono

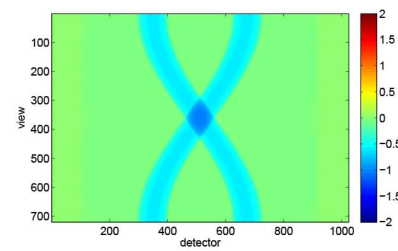

(b) 2-nd order MBIR-BHC

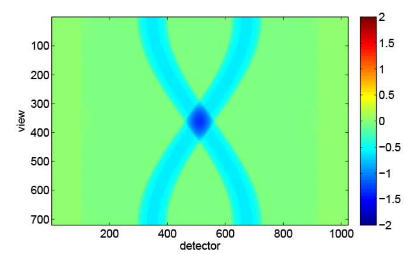

(c) 3-rd order MBIR-BHC

Fig. 6. Comparison of the modeling error for the three forward models of MBIR-mono, MBIR-BHC with a 2-nd order model, and MBIR-BHC with a 3-rd order model. Notice that MBIR-BHC with the second order model produces the smallest modeling error.

TABLE V
QUANTITATIVE COMPARISON OF THE MODELING ERROR

	MBIR-mono	2-nd MBIR-BHC	3-rd MBIR-BHC
absolute mean	0.1187	0.1172	0.1177
variance	0.0476	0.0436	0.0448

where $p_{L,i}$ and $p_{H,i}$ are the projections of low and high density materials of $x^{(\text{phantom})}$ and $\tilde{\gamma}_{k,l}$ are the convergent parameters produced by MBIR-BHC. We study the 2-nd order MBIR-BHC ($p = 2$) and 3-rd order MBIR-BHC ($p = 3$). Fig. 6 compares the modeling error of MBIR-mono and MBIR-BHC. All three methods have visible errors in the trace of high density insertions. Notice that the approximation error by the 2-nd order MBIR-BHC is somewhat smaller than the error for MBIR-mono. However, once again, the 3-rd order MBIR-BHC model is no better than the 2-nd order model. The corresponding quantitative results listed in Table V also show that the 2-nd order MBIR-BHC gives smaller absolute mean and variance of the approximation error than MBIR-mono.

2) Multi-Material Disk Phantom: We continue the simulation study using a multi-material phantom, which

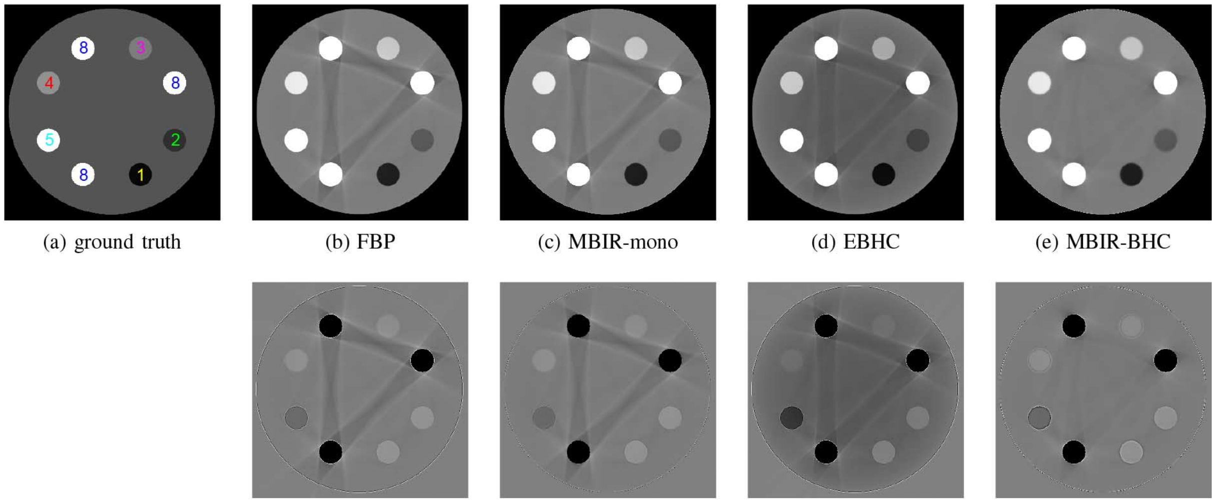

(a) ground truth (b) FBP (c) MBIR-mono (d) EBHC (e) MBIR-BHC

(f) (b) - (a) (g) (c) - (a) (h) (d) - (a) (i) (e) - (a)

Fig. 7. Comparison of FBP, MBIR-mono, EBHC and MBIR-BHC reconstructed images. Top row: the reconstructed images. Bottom row: the difference images. The display window for the reconstructed images is [−200 200] HU. The display window for the difference images is [−200 200] HU. Notice that the MBIR-BHC algorithm reduces visible beam-hardening artifacts in the reconstruction of simulated data.

TABLE VI
CHEMICAL COMPOSITION OF VARIOUS MATERIALS USED IN FIG. 7(A)

cylinder #	material	density (g/cc)	chemical formula
1	polypropylene	0.90	C_3H_6
2	polystyrene	1.05	C_8H_8
3	acrylic	1.2	$C_5H_8O_2$
4	ULTEM	1.32	$C_{37}H_{24}N_2O_6$
5	ETFE	1.7	$C_2H_4 + C_2F_4$
8	PVC	1.4	C_2H_3Cl

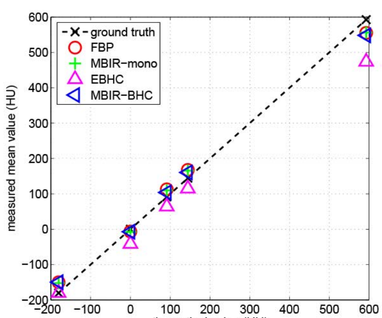

Fig. 8. Comparison of the reconstruction accuracy of FBP, MBIR-mono, EBHC and MBIR-BHC. Ground truth values are calculated using (6). Notice that the MBIR-BHC reconstruction algorithm produces relatively low bias in the reconstructed density.

TABLE VII
VALUES OF THE POLYNOMIAL COEFFICIENTS ESTIMATED BY MBIR-BHC FOR THE EXPERIMENT IN FIG. 9

model	$\tilde{\gamma}_{1,1}$	$\tilde{\gamma}_{0,2}$	$\tilde{\gamma}_{2,1}$	$\tilde{\gamma}_{1,2}$	$\tilde{\gamma}_{0,3}$
2-nd order	0.00945	-0.03231	0	0	0
3-nd order	0.03923	-0.03038	-0.00731	-0.00913	0.00511

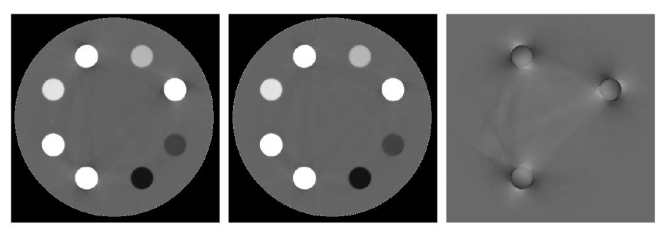

(a) 2-nd order MBIR-BHC (b) 3-rd order MBIR-BHC (c) (b) - (a)

Fig. 9. Comparison of 2-nd order MBIR-BHC and 3-rd order MBIR-BHC. The display window for the reconstructed images is [−200 200] HU. The display window for the difference image is [−50 50] HU. Notice that the 2-nd order model produces good results with lower complexity than the 3-rd order model.

consists of a water disk with radius of 90 mm, with several insertions of radius 10 mm, as shown in Fig. 7(a). The chemical composition of the numbered objects are listed in Table VI.

We first simulate a parallel-beam projection sinogram with 1024 detectors of 0.24 mm and 720 projection angles over 180 degrees. We do not simulate the noise and scatter effects. All the reconstructed images are 512×512 over the 250 mm FOV. For MBIR-BHC, the 2-nd order polynomial model is used and the segmentation threshold T is 800 HU. The reconstruction results using different methods are presented in Fig. 7. Notice that severe streaks through the high density objects are present in FBP and MBIR-mono reconstructions. In the EBHC reconstruction, streaks are suppressed but there are still noticeable artifacts remaining. In contrast, MBIR-BHC significantly reduces the streak artifacts. A corresponding improvement is also observed in the difference images. Fig. 8 shows a comparison of the mean reconstructed values of the objects # 1-5 as compared to the theoretically correct values obtained from equation (6). The three algorithms of FBP, MBIR-mono and MBIR-BHC all produce attenuation coefficients with approximately equal accuracy, while EBHC introduces a bias in the mean reconstructed values.

Using the same simulated data from the multi-material phantom, we further investigate the effect of the order of the polynomial model in MBIR-BHC. Table VII lists the values

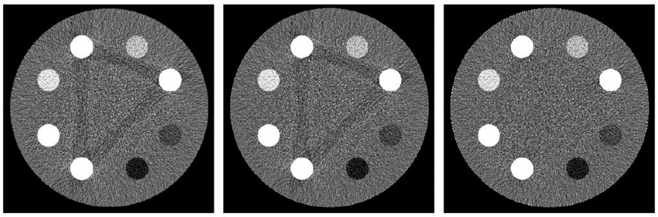

(a) FBP (b) MBIR-mono (c) MBIR-BHC

Fig. 10. Comparison of FBP, MBIR-mono and MBIR-BHC reconstructions on noisy sinogram. The display window for the reconstructed images is [−200 200] HU. Notice that the MBIR-BHC algorithm robustly removes beam-hardening artifacts in the presence of simulated measurement noise.

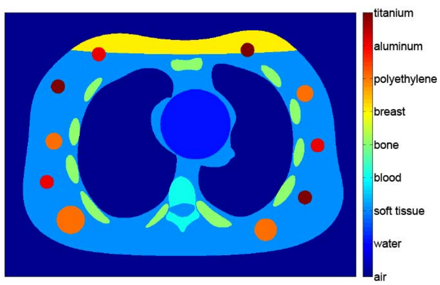

(a) chemical composition

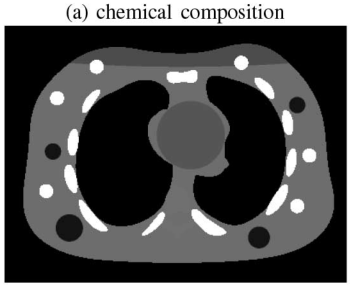

(b) attenuation map

Fig. 11. Material composition of the modified NCAT phantom. Top row: color-coded material composition of the phantom. Bottom row: the attenuation map of the phantom. The display window is [−200, 400] HU.

of the polynomial coefficients estimated by the 2-nd and 3-rd order MBIR-BHC. Fig. 9 compares the result of 2-nd and 3-rd order models for MBIR-BHC. By visual comparison, the 3-rd order MBIR-BHC reconstruction is slightly better than the 2-nd order result and the subtle improvement can be also noticed in the difference image. However, increasing parameters in higher order models may lead to the over-fitting of the projection data and also requires more computation. In practice, we have found that the 2-nd order MBIR-BHC model is sufficient to provide good results.

Fig. 10 illustrates the robustness of the MBIR-BHC algorithm to sensor noise using the multi-material disk phantom. Our simulated data uses independent additive Gaussian noise with inverse variances given by (35) using $\lambda_{0,i} = 20000$ for all $i = 1, \ldots, M$ and $\sigma_e^2 = 16$. For the purposes of this particular comparison, we adjust the regularization in the MBIR-mono and MBIR-BHC to approximately match the noise variance of FBP. In practice, this means that the MBIR reconstructions are under-regularized since generally speaking MBIR can produce the same resolution as FPB at lower noise levels. Notice that

TABLE VIII
CHEMICAL COMPOSITION OF VARIOUS MATERIALS USED IN THE SIMULATION

material	density (g/cc)	chemical composition
water	1.0	H_2O
soft tissue	1.06	H: 10.2%, C: 14.3%, N: 3.4%, O: 70.8%, Na: 0.2%, P: 0.3%, S: 0.3%, Cl: 0.2%, K: 0.3%
blood	1.06	H: 10.2%, C: 11.0%, N: 3.3%, O: 74.5%, Na: 0.1%, P: 0.1%, S: 0.2%, Cl: 0.3%, K: 0.2%, Fe: 0.1%
bone	1.92	H: 3.4%, C: 15.5%, N: 4.2%, O: 43.5%, Na: 0.1%, Mg: 0.2%, P: 10.3%, S: 0.3%, Ca: 22.5%
breast	1.02	H: 10.6%, C: 33.2%, N: 3.0%, O: 52.7%, Na: 0.1%, P: 0.1%, S: 0.2%, Cl: 0.1%
polyethylene	0.93	H: 14.372%, C: 85.628%
aluminum	2.7	Al
titanium	4.506	Ti

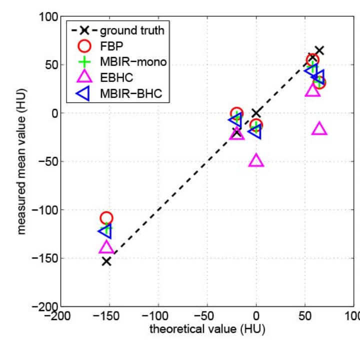

(a) low attenuation region

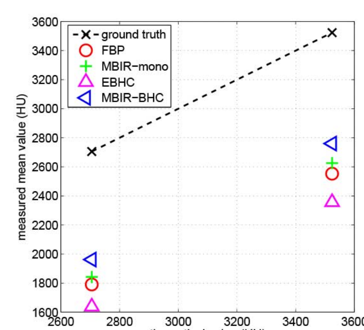

(b) high attenuation region

Fig. 12. Comparison of the reconstruction accuracy of FBP, MBIR-mono, EBHC and MBIR-BHC on NCAT phantom. Ground truth values are calculated using (6). Notice that the MBIR-BHC reconstruction algorithm produces the lowest bias in estimated density among the tested algorithms.

both the FBP and MBIR-mono reconstructions contain streaks, while the MBIR-BHC effectively removes the streak artifacts even in the presence of noise.

3) Modified NCAT Phantom: The third phantom we investigate is based on the NCAT phantom [48]. It has a FOV of 320 mm, and we manually inserted several regions of high and

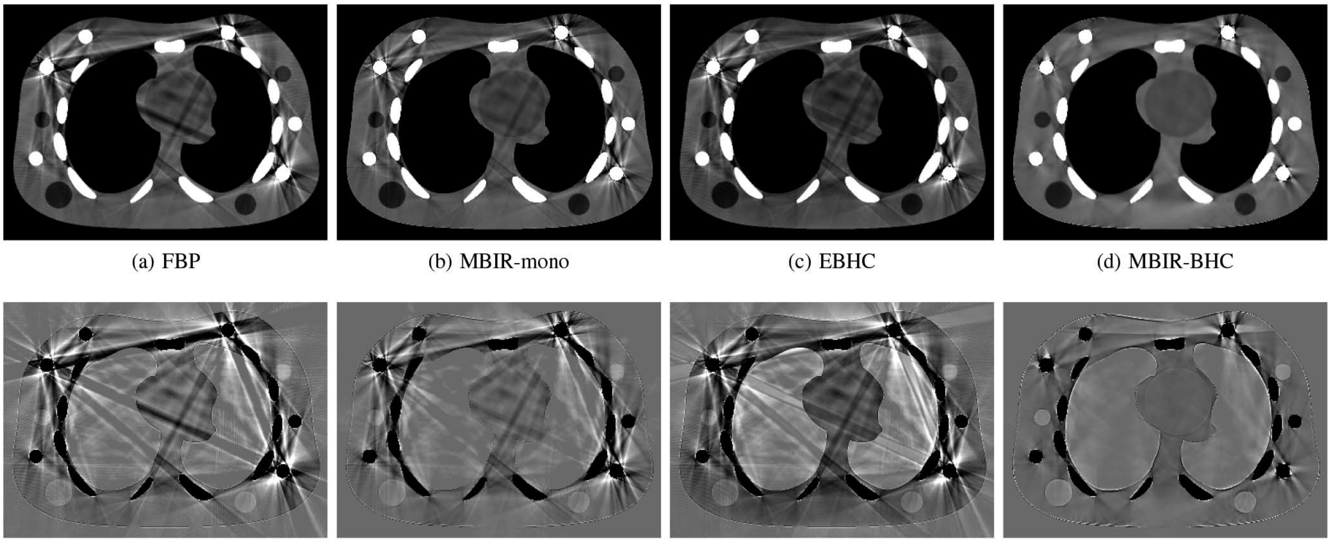

(a) FBP (b) MBIR-mono (c) EBHC (d) MBIR-BHC

(e) Difference: (a) - 11(b) (f) Difference: (b) - 11(b) (g) Difference: (c) - 11(b) (h) Difference: (d) - 11(b)

Fig. 13. Comparison of FBP, the generic MBIR with mono-energetic X-ray model (MBIR-mono), and MBIR-BHC reconstructed images. First row: the reconstructed images. Second row: the difference images. The display window for the reconstructed images is [−200 400] HU. The display window for the difference images is [−200 200] HU. Notice that the MBIR-BHC algorithm reduces visible beam-hardening artifacts in the reconstruction of the simulated human phantom.

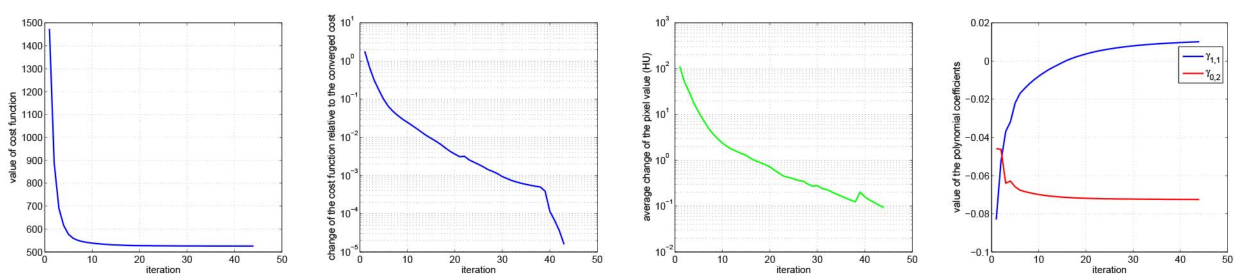

(a) cost (b) cost change relative to the converged cost (c) average pixel change (d) polynomial coefficients

Fig. 14. Convergence of MBIR-BHC algorithm. The plots show (a) value of the exact objective function of (40); (b) the change of the objective function relative to the converged value; (c) the average change of pixel value; and (d) estimated polynomial coefficients, after each iteration.

low density materials, such as soft tissue, bone, blood and metals, indicated in Fig. 11. The densities and the mass attenuation coefficients of the materials used in the phantoms are obtained from the NIST XCOM database [49] and the chemical compositions of these materials are listed in Table VIII according to [50].

The simulated parallel-beam geometry has 1400 detectors with 0.23 mm spacing and 720 projection angles over 180 degrees. We do not simulate the noise and scatter effects. All the reconstructed images are 512×512. For MBIR-BHC, the 2-nd order polynomial model is used and the segmentation threshold T is 800 HU. The reconstruction results are shown in Fig. 13.

Due to the presence of high density metal insertions, the FBP reconstruction exhibits several streaking artifacts crossing through the image, which degrades the overall image quality. While the generic MBIR-mono reconstruction generally improves the image quality and smooths out several degraded regions, it fails to eliminate the streaks connecting the high density regions, such as bone and metal. The EBHC method is not as effective on this data set, probably due to the presence of multiple high density objects. By comparison, the MBIR-BHC method dramatically reduces most of the streaking artifacts, while producing a better rendering in uniform regions and preserving the shape of edges as well. The difference between the reconstruction and the ground truth also demonstrates the effectiveness of MBIR-BHC in removing streaks. We also plot the mean pixel values of different regions in the phantom versus their theoretical values in Fig. 12. In the low attenuation region, FBP, MBIR-mono and MBIR-BHC give roughly equal accuracy estimate, while EBHC tends to under estimate the pixel value. In the high attenuation regions, all the methods produce lower accuracy estimates of density, but the MBIR-BHC method produces the most accurate results.

B. Real Scan Data Results

In this section, we apply different methods to a real X-ray CT scan dataset taken of actual baggage with high and low density objects. The dataset is acquired from the Imatron C300 CT scanner, provided by the ALERT DHS center, Northeastern University, USA. The parallel-beam sinogram has 1024 detectors with 0.46 mm spacing and 720 projection angles over 180

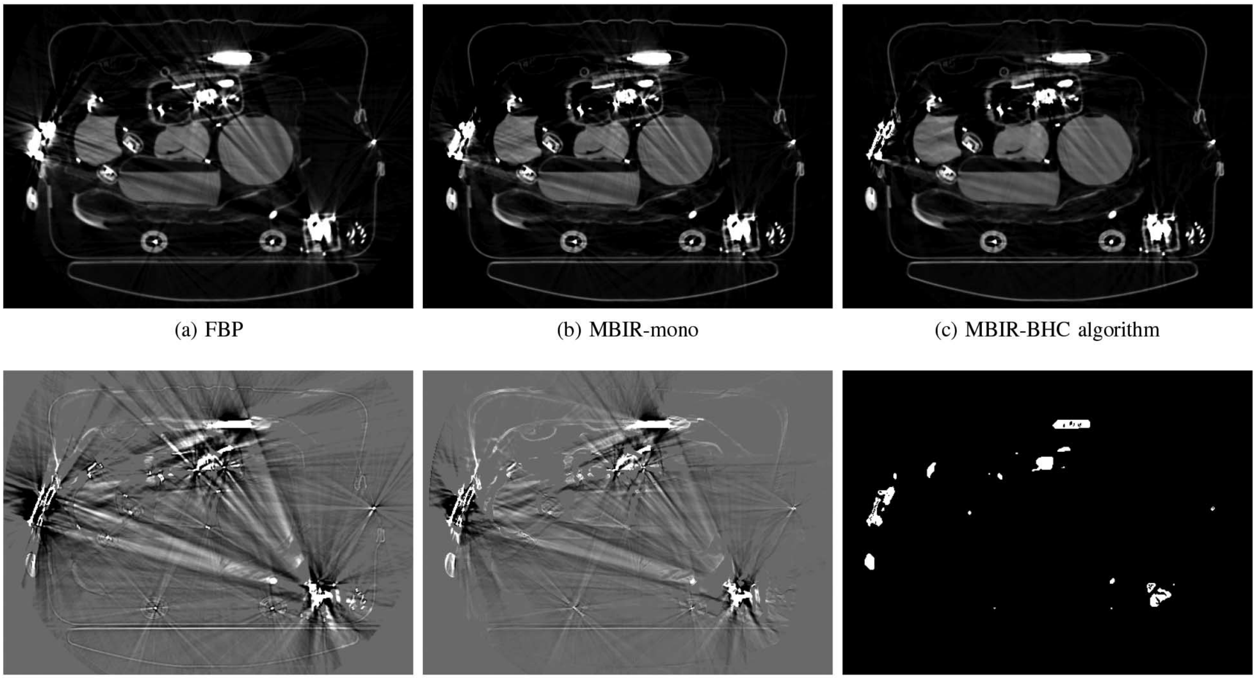

(a) FBP (b) MBIR-mono (c) MBIR-BHC algorithm

(d) Difference: (c) - (a) (e) Difference: (c) - (b) (f) MBIR-BHC segmentation mask

Fig. 15. Comparison of FBP, the generic MBIR with mono-energetic X-ray model (MBIR-mono), MBIR-BHC, on the real X-ray CT data of a scanned baggage. Top row: the reconstructed images. Bottom row shows the segmentation mask of MBIR-BHC and difference images between MBIR-BHC and FBP, difference between MBIR-BHC and MBIR-mono. The display window for the reconstructed images (a)-(c) is $[-1000, 1000]$ HU. The display window for the difference images (d)-(e) is $[-500, 500]$ HU In (d), white pixels indicate the pixels which are classified as the high density materials in MBIR-BHC. Notice that the MBIR-BHC algorithm reduces visible beam-hardening artifacts such as streaking on this real data set.

degrees, rebinned from a fan-beam scan. The projection data is water pre-corrected. The reconstructed images have a FOV of 475 mm with the resolution of 512×512. We use the 2-nd order MBIR-BHC and choose the segmentation threshold T to be 800 HU.

We first investigate the convergence behavior of the MBIR-BHC algorithm. Fig. 14(a) plots the objective function after each iteration of optimization over x, b and γ. As we have described in Section III, the objective function (40) is approximated by the quadratic approximation (43) using the second order Taylor series expansion with the expansion point iteratively refined during the reconstruction. While we point out that this approximation is not guaranteed to be an upper bound of the original objective function, which would ensure the convergence, we see from Fig. 14(a) that in practice the objective function decreases, which suggests that the proposed strategy is effective for this high order non-linear optimization problem, and yields convergent results empirically. In Fig. 14(b), we plot the change of the objective function relative to the converged value on a log scale, given by

$$\log\left(\frac{\text{cost}^{(t)} - \text{cost}^{(\infty)}}{\text{cost}^{(\infty)}}\right) \tag{64}$$

where $\text{cost}^{(\infty)}$ is the converged value of the objective function. Note that the change is also monotonic decreasing. Fig. 14(c) plots the average pixel change after each iteration in log scale. and Fig. 14(d) plots the coefficients of the correction polynomial after each iteration. As shown in the figures, the average pixel change decreases to zero and the coefficients of the polynomial converge to a stable estimate after a few iterations.

Fig. 15 shows the reconstruction results of this baggage scan dataset using different methods. By visual comparison to FBP and generic MBIR-mono, the MBIR-BHC method reduces the streaking and blooming artifacts significantly and produces reconstructions with higher resolution. This can be clearly observed in the zoomed-in region in Fig. 16. The metal baggage handle causes a severe blooming artifact in the FBP image, and affects the nearby low density uniform regions as well. While the generic MBIR-mono algorithm recovers a few structures with better detail, it does not effectively address the artifacts due to the metal and many streaks remain on the final reconstructed image. On the other hand, the MBIR-BHC algorithm was able to produce more accurate and clearer structures. The streaking artifacts in the uniform attenuation regions, caused by the nearby high-density metal, are significantly reduced in the reconstructed images of the MBIR-BHC algorithm. Also, MBIR-BHC improves the overall resolution. Fig. 15(d) illustrates the segmentation mask of MBIR-BHC after the reconstruction is finished. It can be observed that the algorithm correctly identifies the high density regions and eliminates the segmentation noise.

We also include the normalized error sinograms obtained from the generic MBIR-mono and MBIR-BHC algorithms in Fig. 17 which illustrates the improvement of MBIR-BHC due

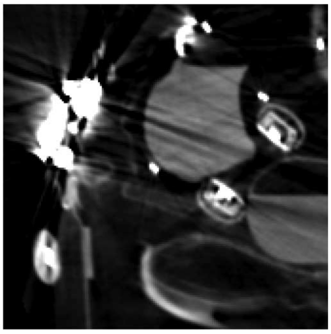

(a) FBP

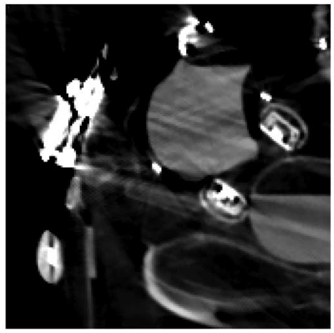

(b) MBIR-mono

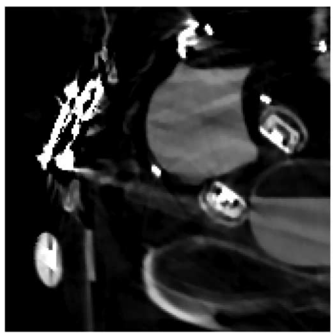

(c) MBIR-BHC

Fig. 16. Comparison of FBP, MBIR-mono, MBIR-BHC on the real X-ray CT data of a scanned baggage. Images are zoomed-in a region including metal objects. The display window is $[-1000, 1000]$ HU. Notice that the MBIR-BHC reconstructions have reduced streaking, more uniform homogeneous regions, and less blooming of metal in this real data set.

to the proposed X-ray model with the polynomial parametrization. The normalized error sinogram is the difference between the sinogram data and the forward projection of the image, normalized by the weighting coefficients. If the forward model is correct and the reconstruction is a least-weighted-squares fit to the data, this normalized error should appear as approximately white noise with unit variance across the sinogram. Mathematically, for the generic MBIR algorithm, the normalized error sinogram is calculated as

$$e_i^{(\text{MBIR-mono})} = \sqrt{w_i}\left(y_i - \sum_{j=1}^{N} A_{i,j}x_j\right), \tag{65}$$

and for the proposed MBIR-BHC algorithm, it is

$$e_i^{(\text{MBIR-BHC})} = \sqrt{w_i}(y_i - p_i). \tag{66}$$

As seen from the figure, the MBIR-BHC shows a more uniform normalized error sinogram map with less fluctuation. Several traces due to the presence of the metal in the error sinogram of MBIR-mono nearly disappear in MBIR-BHC.

As seen from the results, MBIR-BHC has improved the overall image quality and significantly reduced the streaking artifacts due to beam hardening of the high density materials. Nonetheless, MBIR-BHC does not remove all beam-hardening artifacts. The remaining artifacts may be due to various reasons, including inaccurate modeling. For real scan data, other physical effects, such as scattering, may also influence the results.

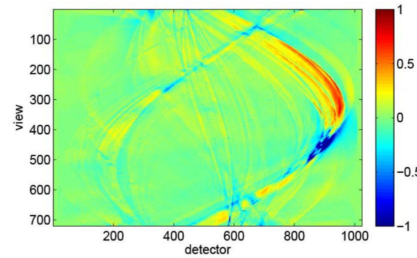

(a) MBIR-mono

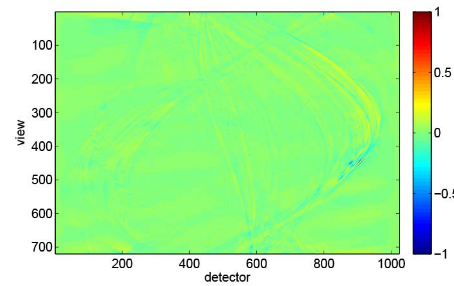

(b) MBIR-BHC

Fig. 17. Comparison of MBIR-mono and MBIR-BHC on the normalized error sinogram

While Fig. 6 indicates that the 2-nd order MBIR-BHC forward model is more accurate, the 3-rd order model shows little further improvement.

V. Conclusion

In this paper, we have presented a model-based iterative method for simultaneous image reconstruction and beam hardening correction (MBIR-BHC) which does not require any prior knowledge of the nonlinear characteristics of the system. The main idea is to jointly estimate the reconstruction and the beam hardening correction polynomial using an alternating optimization approach. The method is based on the assumption that distinct materials can be separated according to their densities. Under this assumption, the proposed method simultaneously estimates the reconstruction, the material segmentation mask, and the joint polynomial correction function of different material projections. Two separated projections are computed implicitly based on the low and high density materials during the iterative process. Therefore, no system information is needed and the correction is adapted to the dataset being used automatically. The experimental results on both the simulated and real dataset demonstrated the efficiency of the proposed algorithm in reducing several artifacts in the reconstructed image, such as streaking.

Appendix A
Derivations of the Relationships in Section II

In this appendix, we derive the equations (14), (24)–(25), and (29)–(31) in Section II.

To see (14), we differentiate (11) and obtain

$$\begin{aligned}\frac{d}{dp_i} f_{\mathcal{M}}(p_i)|_{p_i=0} &= -\frac{\int_{\mathbb{R}} \tilde{S}(\mathcal{E}) \frac{d}{dp_i} e^{-r_{\mathcal{M}}(\mathcal{E})p_i} d\mathcal{E}}{\int_{\mathbb{R}} \tilde{S}(\mathcal{E}) e^{-r_{\mathcal{M}}(\mathcal{E})p_i} d\mathcal{E}}|_{p_i=0} \\ &= \frac{\int_{\mathbb{R}} \tilde{S}(\mathcal{E}) e^{-r_{\mathcal{M}}(\mathcal{E})p_i} r_{\mathcal{M}}(\mathcal{E}) d\mathcal{E}}{\int_{\mathbb{R}} \tilde{S}(\mathcal{E}) e^{-r_{\mathcal{M}}(\mathcal{E})p_i} d\mathcal{E}}|_{p_i=0} \\ &= \int_{\mathbb{R}} \tilde{S}(\mathcal{E}) r_{\mathcal{M}}(\mathcal{E}) d\mathcal{E} = 1\end{aligned}$$

where the last equality is the result of (9).

To see (24), we differentiate (19) and obtain

$$\begin{aligned}\gamma_{1,0} &= \frac{\partial}{\partial p_{L,i}} h(p_{L,i}, 0)|_{p_{L,i}=0} \\ &= -\frac{\partial}{\partial p_{L,i}} \log\left(\int_{\mathbb{R}} \tilde{S}(\mathcal{E}) e^{-r_L(\mathcal{E})p_{L,i}} d\mathcal{E}\right)|_{p_{L,i}=0} \\ &= \frac{\int_{\mathbb{R}} \tilde{S}(\mathcal{E}) e^{-r_L(\mathcal{E})p_i} r_L(\mathcal{E}) d\mathcal{E}}{\int_{\mathbb{R}} \tilde{S}(\mathcal{E}) e^{-r_L(\mathcal{E})p_i} d\mathcal{E}}|_{p_{L,i}=0} \\ &= \int_{\mathbb{R}} \tilde{S}(\mathcal{E}) r_L(\mathcal{E}) d\mathcal{E} = 1\end{aligned}$$

and (25) can be derived in the similar manner, changing the differentiation with respect to $p_{H,i}$.

For (29), plugging $p_{L,i} = p_{H,i} = 0$ into (27), we obatin

$$\tilde{\gamma}_{0,0} = f_{\mathcal{M}}^{-1}\left(-\log\left(\int_{\mathbb{R}} \tilde{S}(\mathcal{E}) e^0 d\mathcal{E}\right)\right) = f^{-1}(0) = 0. \quad (67)$$

Finally, to see (30), we apply the chain rule using (15) and (24) and obtain

$$\begin{aligned}\tilde{\gamma}_{1,0} &= \frac{\partial}{\partial p_{L,i}} \tilde{h}(p_{L,i}, 0)|_{p_{L,i}=0} \\ &= \frac{df_{\mathcal{M}}^{-1}(h(p_{L,i}, 0))}{dh(p_{L,i}, 0)} \frac{\partial}{\partial p_{L,i}} h(p_{L,i}, 0)|_{p_{L,i}=0} \\ &= \int_{\mathbb{R}} \tilde{S}(\mathcal{E}) r_L(\mathcal{E}) d\mathcal{E} = 1\end{aligned}$$

and (31) can be derived in the similar manner, changing the differentiation with respect to $p_{H,i}$.

Appendix B
Derivation of the ICD Update Equations

In this appendix, we derive the ICD pixel update in detail. We rewrite (40) as a function of the pixel x_j, drop the terms which are independent of x_j, and obtain the 1D optimization problem over x_j given by

$$\begin{aligned}x_j = \arg\min_{u \geq 0} \Bigg\{ & \theta_1(u - \tilde{x}_j) + \frac{1}{2}\theta_2(u - \tilde{x}_j)^2 \\ & + \beta\left((u - T)_+(1 - b_j) + (T - u)_+ b_j\right) \\ & + \sum_{k \in \partial j} \alpha_{j,k} \rho(u - x_k) \Bigg\} \end{aligned} \quad (68)$$

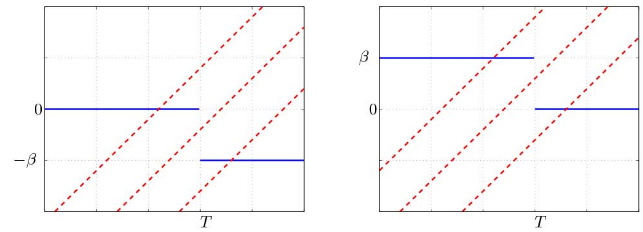

(a) $b_j = 0$ (b) $b_j = 1$

Fig. 18. Illustration of the solutions of (74) and (75). The blue solid lines depict the right side of the normal equations. The red dashed lines depict the left side of the normal equations for different D_1 and D_2. The solutions are the intersections of the blue and red lines.

where $\tilde{x}_j$ is the previous pixel value and θ_1 and θ_2 are given by (49) and (50). Following the similar strategy in [36], we simplify the optimization by replacing the function ρ with a quadratic substitute functional q given by

$$q(u - x_k; \tilde{x}_j - x_k) = a_{j,k}(u - x_k)^2 + C_{j,k} \quad (69)$$

where $a_{j,k}$ and $C_{j,k}$ are given by

$$a_{j,k} = \frac{\rho'(\tilde{x}_j - x_k)}{2(\tilde{x}_j - x_k)}, \quad (70)$$

$$C_{j,k} = \rho(\tilde{x}_j - x_k) - \frac{a_{j,k}}{2}(\tilde{x}_j - x_k)^2. \quad (71)$$

It can be easily shown that this function q is an upper bound of ρ, satisfying the two constraints given by

$$q(u - x_k; \tilde{x}_j - x_k) \geq \rho(u - x_k), \quad (72)$$

$$q(\tilde{x}_j - x_k; \tilde{x}_j - x_k) = \rho(\tilde{x}_j - x_k). \quad (73)$$

Therefore, such substitution will not alter the optimal solution when the algorithm converges. Substituting (69) into (68) and dropping the terms which do not depend on u, we obtain the 1D optimization (47) with $\alpha'_{j,k}$ given by (48).

To derive the optimal solution to (47), we separate the cases when $b_j = 0$ or 1. We first suppose $b_j = 0$ and zero the derivative of (47) to obtain the normal equation given by

$$\begin{aligned}\theta_1 - \theta_2\tilde{x}_j - 2\sum_{k \in \partial j} \alpha'_{j,k} x_k + \left(\theta_2 + 2\sum_{k \in \partial j} \alpha'_{j,k}\right) u & \\ = -\beta \text{step}(u - T) & \\ D_1 + D_2 u = -\beta \text{step}(u - T) &\end{aligned} \quad (74)$$

where step$(\cdot)$ is the unit step function, and D_1 and D_2 are given by (51) and (52). The solution to (74) can be obtained using the shrinkage operator in solving LASSO and l_1 regularized problems [51], and the closed form solution is given by (53). For the case when $b_j = 1$, we have the normal equation given by

$$D_1 + D_2 u = \beta \text{step}(T - u). \quad (75)$$

and the update equation in this case becomes (55). Fig. 18 illustrates these two cases graphically.

ACKNOWLEDGMENT

The authors would like to thank the ALERT DHS center, Northeastern University for their support of this research. They also thank Dr. C. Crawford for providing useful information and discussion. The X-ray spectrum information is the courtesy of Dr. T. Gilat-Schmidt from Marquette University.

REFERENCES

[1] J. D. Ingle and S. R. Crouch, *Spectrochemical Analysis*, 1st ed. Englewood, Cliffs, NJ, USA: Prentice Hall, 1988.
[2] R. A. Brooks and G. D. Chiro, "Beam hardening in X-ray reconstructive tomography," *Phys. Med. Biol.*, vol. 21, no. 3, pp. 390–398, 1976.
[3] J. Hsieh, *Computed Tomograhpy: Principles, Design, Artifacts, and Recent Advances*, 2nd ed. Hoboken, NJ, USA: Wiley, 2009, ch. 7, pp. 270–279.
[4] W. D. McDavid, R. G. Waggener, W. H. Payne, and M. J. Dennis, "Spectral effects on three-dimensional reconstruction form X-rays," *Med. Phys.*, vol.. 2, no. 6, pp. 321–324, 1975.
[5] L. M. Zatz and R. E. Alvarez, "An inaccuracy in computed tomography: The energy-dependence of CT values," *Radiology*, vol. 124, no. 1, pp. 91–97, Jul. 1977.
[6] A. J. Duerinckx and A. Macovski, "Polychromatic streak artifacts in computer tomography images," *J. Comput. Assist. Tomogr.*, vol. 2, no. 4, pp. 481–487, Sep. 1978.
[7] P. S. Rao and R. J. Alfidi, "The environmental density artifact: A beam-hardening effect in computed tomography," *Radiology*, vol. 141, no. 1, pp. 223–227, Oct. 1981.
[8] W. D. McDavid, R. G. Waggener, W. H. Payne, and M. J. Dennis, "Correction for spectral artifacts in cross-sectional reconstruction from X rays," *Med. Phys.*, vol. 4, no. 1, pp. 54–57, 1977.
[9] S. C. Pang and S. Genna, "Correction for X-ray polychromaticitiy effects on three-dimensional reconstruction," *IEEE Trans. Nucl. Sci.*, vol. 23, no. 1, pp. 623–626, Feb. 1976.
[10] G. T. Herman, "Correction for beam hardening in computed tomography," *Phys. Med. Biol.*, vol. 24, no. 1, pp. 81–106, 1979.
[11] R. E. Alvarez and A. Macovski, "Energy-selective reconstructions in X-ray computerized tomography," *Phys. Med. Biol.*, vol. 21, no. 5, pp. 733–744, 1976.
[12] J. P. Stonestrom, R. E. Alvarez, and A. Macovski, "A framework for spectral artifact corrections in X-ray CT," *IEEE Trans. Biomed. Eng.*, vol. 28, no. 2, pp. 128–141, Feb. 1981.
[13] P. M. Joseph and R. D. Spital, "A method for correcting bone induced artifacts in computed tomography scanners," *J. Comput. Assist. Tomogr.*, vol. 20, no. 10, pp. 100–108, Jan. 1978.
[14] Y. Censor, T. Elfving, and G. Herman, "A method of iterative data refinement and its applications," *Math. Methods Appl. Sci.*, vol. 7, pp. 108–123, 1985.
[15] G. Herman and S. Trivedi, "A comparative study of two postreconstruction beam hardening correction methods," *IEEE Trans. Med. Imag.*, vol. 2, no. 3, pp. 128–135, Sep. 1983.
[16] P. M. Joseph and C. Ruth, "A method for simultaneous correction of spectrum hardening artifacts in CT images containing both bone and iodine," *Med. Phys.*, vol. 24, no. 10, pp. 1629–1634, Oct. 1997.
[17] J. Hsieh, R. Molthen, C. A. Dawson, and R. H. Johnson, "An iterative approach to the beam hardening correction in cone beam CT," *Med. Phys.*, vol. 27, no. 1, pp. 23–29, Jan. 2000.
[18] A. J. Coleman and M. Sinclair, "A beam-hardening correction using dual-energy computed tomography," *Phys. Med. Biol.*, vol. 30, no. 11, pp. 1251–1256, 1985.
[19] R. J. Jennings, "A method for comparing beam-hardening filter materials for diagnostic radiology," *Med. Phys.*, vol. 15, no. 4, pp. 588–599, 1988.
[20] O. Nalcioglu and R. Y. Lou, "Post-reconstruction method for beam hardening in computerised tomography," *Phys. Med. Biol.*, vol. 24, no. 2, pp. 330–340, 1979.
[21] C. H. Yan, R. T. Whalen, G. S. Beaupré, S. Y. Yen, and S. Napel, "Reconstruction algorithm for polychromatic CT imaging: Application to beam hardening correction," *IEEE Trans. Med. Imag.*, vol. 19, no. 1, pp. 1–11, Jan. 2000.
[22] B. D. Man, J. Nuyts, P. Dupont, G. Marchal, and P. Suetens, "An iterative maximum-likelihood polychromatic algorithm for CT," *IEEE Trans. Med. Imag.*, vol. 20, no. 10, pp. 998–1008, Oct. 2001.
[23] I. A. Elbakri and J. A. Fessler, "Statistical X-ray computed tomography image reconstruction with beam hardening correction," in *Proc. SPIE Conf. Med. Imag. Image Process.*, 2001, vol. 4322.
[24] I. A. Elbakri and J. A. Fessler, "Segmentation-free statistical image reconstruction for polyenergetic X-ray computed tomography with experimental validation," *Phys. Med. Biol.*, vol. 48, pp. 2453–2477, Aug. 2003.
[25] E. V. de Casteele, D. V. Dyck, J. Sijbers, and E. Raman, "A model-based correction method for beam hardening artefacts in X-ray microtomograhpy," *J. X-Ray Sci. Technol.*, vol. 12, no. 1, pp. 43–57, 2004.
[26] S. Srivastava and J. A. Fessler, "Simplified statistical image reconstruction algorithm for polyenergetic X-ray CT," in *Proc. IEEE Nucl. Sci. Symp.*, 2005, pp. 1551–1555.
[27] M. Kachelrieß, K. Sourbella, and W. A. Kalender, "Empirical cupping correction: A first-order raw data pre-correction for cone-beam computed tomography," *Med. Phys.*, vol. 37, no. 5, pp. 1269–1274, May 2006.
[28] H. Gao, L. Zheng, Z.-Q. Chen, Y. Xing, and S. Li, "Beam hardening correction for middle-energy industrial computerized tomograhpy," *IEEE Trans. Nucl. Sci.*, vol. 53, no. 5, pp. 2796–2807, Oct. 2006.
[29] M. Krumm, K. Kasperl, and M. Franz, "Reducing non-linear artifacts of multi-material objects in industrial 3d computed tomography," *NDT E Int.*, vol. 41, no. 4, pp. 242–251, 2008.
[30] M. Abella and J. A. Fessler, "A new statistical image reconstruction algorithm for polyenergetic X-ray CT," in *Proc. IEEE Int. Symp. Biomed. Imag.*, 2009, pp. 165–168.
[31] Y. Kyriakou, E. Meyer, D. Prell, and M. Kachelrieß, "Empirical beam hardening correction (EBHC) for CT," *Med. Phys.*, vol. 37, no. 10, pp. 5179–5187, Oct. 2010.
[32] M. Krumm, K. Kasperl, and M. Franz, "Beam hardening correction of multi-material objects," in *Proc. 10th Eur. Conf. Non-Destruct. Test.*, 2010.
[33] J. M. Verburg and J. Seco, "CT metal artifact reduction method correcting for beam hardening and missing projections," *Phys. Med. Biol.*, vol. 57, pp. 2803–2818, Apr. 2012.
[34] P. Jin, "Model-based image processing algorithms for CT image reconstruction, artifact reduction and segmentation," Ph.D. dissertation, Purdue Univ., West Lafayette, IN, USA, Aug. 2015.
[35] J.-B. Thibault, K. D. Sauer, C. A. Bouman, and J. Hsieh, "A three-dimensional statistical approach to improved image quality for multi-slice helical CT," *Med. Phys.*, vol. 34, no. 11, pp. 4526–4544, Nov. 2007.
[36] Z. Yu, J.-B. Thibault, C. A. Bouman, K. D. Sauer, and J. Hsieh, "Fast model-based X-ray CT reconstruction using spatially nonhomogenenous ICD optimization," *IEEE Trans. Image Process.*, vol. 20, no. 1, pp. 161–175, Jan. 2011.
[37] R. Zhang, J.-B. Thibault, C. A. Bouman, K. D. Sauer, and J. Hsieh, "Model-based iterative reconstruction for dual-energy X-ray CT using a joint quadratic likelihood model," *IEEE Trans. Med. Imag.*, vol. 33, no. 1, pp. 117–134, Jan. 2014.
[38] S. J. Kisner *et al.*, "Innovative data weighting for iterative reconstruction in a helical ct security baggage scanner," in *Proc. IEEE Int. Carnahan Conf. Sec. Technol.*, Medellín, Colombia, 2013, pp. 1–5.
[39] P. Jin, E. Haneda, C. A. Bouman, and K. D. Sauer, "A model-based 3D multi-slice helical CT reconstruction algorithm for transportation security application," in *Proc. 2nd Int. Meeting Image Format. X-Ray CT*, 2012, pp. 297–300.
[40] P. Jin, C. A. Bouman, and K. D. Sauer, "A method for simultaneous image reconstruction and beam hardening correction," in *Proc. Conf. Rec. IEEE Nucl. Sci. Symp. Med. Imag. Conf.*, Seoul, Korea, Nov. 2013, pp. 1–5.
[41] X. Wu, P. U. Simoni, T. L. Toth, and N. B. Bromberg, "Method and apparatus for correcting for beam hardening in CT images," U.S. Patent 7 391 844 B2, Jun. 24, 2005 [Online]. Available: http://www.google.com/patents/US7391844
[42] A. Mohammad-Djafari, "Joint estimation of parameters and hyperparameters in a bayesian approach of solving inverse problems," in *Proc. IEEE Int. Conf. Image Proc.*, Lausanne, Switzerland, Sep. 1996, vol. 2, pp. 473–476.
[43] P. Jin, D. H. Ye, and C. A. Bouman, "Joint metal artifact reduction and segmentation of CT images using dictionary-based image prior and continuous-relaxed Potts model," in *Proc. IEEE Int. Conf. Image Proc.*, Québec City, QC, Canada, Sep. 2015.
[44] C. A. Bouman. (2015). *Model Based Image Processing* [Online]. Available: https://engineering.purdue.edu/˜bouman/publications/pdf/MBIP-book.pdf
[45] A. B. Milstein *et al.*, "Fluorescence optical diffusion tomography," *Appl. Opt.*, vol. 42, no. 16, pp. 3081–3094, Jun. 2003.

[46] P. Jin, E. Haneda, and C. A. Bouman, "Implicit Gibbs prior models for tomographic reconstruction," in *Proc. 46th Asilomar Conf. Signals Syst. Comput.*, Pacific Grove, CA, USA, Nov. 2012, pp. 613–616.

[47] K. Cranley, B. J. Gilmore, G. W. A. Fogarty, and L. Deponds, "Catalogue of diagnostic X-ray spectra and other data," *IPEM Report, Inst. Phys. Eng. Med.*, York, U.K., Tech. Rep. 78, 1997.

[48] W. P. Segars, M. Mahesh, T. J. Beck, E. C. Frey, and B. M. W. Tsui, "Realistic CT simulation using the 4D XCAT phantom," *Med. Phys.*, vol. 35, no. 8, pp. 3800–3808, Aug. 2008.

[49] NIST. (1996). *Tables of X-Ray Mass Attenuation Coefficients and Mass Energy Absorption Coefficients* [Online]. Available: http://www.nist.gov/pml/data/xraycoef/index.cfm

[50] ICRU, "Tissue substitutes in radiation dosimetry and measurement," *ICRU Report, Int. Commission Radiat. Units Meas.*, Bethesda, MD, USA, Tech. Rep. 44, 1989.

[51] R. Tibshirani, "Regression shrinkage and selection via the Lasso," *J. R. Statist. Soc.*, vol. 58, no. 1, pp. 267–288, 1996.

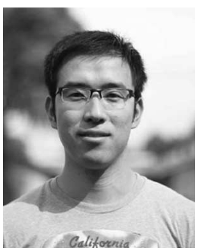

Pengchong Jin received the Bachelor of Engineering degree in electronic and computer engineering (with the first class Hons.) from the Hong Kong University of Science and Technology (HKUST), Hong Kong, in 2009, and the Ph.D. degree in electrical and computer engineering from Purdue University, West Lafayette, IN, USA, in 2015. In Summer 2014, he was interned at Google Inc., Mountain View, CA, USA, working on video processing research. His research interests include image processing, computational imaging, computer vision and machine learning with applications in tomography, camera and photography.

Charles A. Bouman (S'86–M'89–SM'97–F'01) received the B.S.E.E. degree from the University of Pennsylvania, Philadelphia, PA, USA, in 1981, the M.S. degree from the University of California at Berkeley, Berkeley, CA, USA, in 1982, and the Ph.D. degree in electrical engineering from Princeton University, Princeton, NJ, USA, in 1989. From 1982 to 1985, he was a Full Staff Member with MIT Lincoln Laboratory, Lexington, MA, USA. He joined the Faculty of Purdue University, West Lafayette, IN, USA, in 1989 where he is currently the Showalter Professor of Electrical and Computer Engineering and Biomedical Engineering. He also is a Founding Co-Director of Purdue Magnetic Resonance Imaging Facility located in Purdue Research Park. His research interests include the use of statistical image models, multiscale techniques, and fast algorithms in applications including tomographic reconstruction, medical imaging, and document rendering and acquisition. Prof. Bouman is a Fellow of the American Institute for Medical and Biological Engineering (AIMBE), a Fellow of the society for Imaging Science and Technology (IS&T), a Fellow of the SPIE professional society. He was previously the Editor-in-Chief for the IEEE TRANSACTIONS ON IMAGE PROCESSING and a Distinguished Lecturer for the IEEE Signal Processing Society, and he is currently the Vice President of Technical Activities for IEEE Signal Processing Society. He has been an Associate Editor for the IEEE TRANSACTIONS ON IMAGE PROCESSING and the IEEE TRANSACTIONS ON PATTERN ANALYSIS AND MACHINE INTELLIGENCE. He has also been a Co-Chair of the 2006 SPIE/IS&T Symposium on Electronic Imaging, Co-Chair of the SPIE/IS&T conferences on Visual Communications and Image Processing 2000 (VCIP), a Vice President of Publications and a member of the Board of Directors for the IS&T Society, and he is the founder and Co-Chair of the SPIE/IS&T conference on Computational Imaging. He is the recipient of IS&Ts Raymond C. Bowman Award for outstanding contributions to digital imaging education and research, has been a Purdue University Faculty Scholar, the College of Engineering Engagement/Service Award, Team Award, and the Electronic Imaging Scientist of the Year award in 2014.

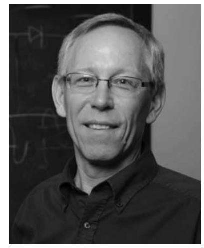

Ken D. Sauer (S'85–M'89) received the B.S.E.E. and the M.S.E.E. degrees from Purdue University, West Lafayette, IN, USA, in 1984 and 1985, and the Ph.D. degree in electrical engineering, as an AT&T Foundation Fellow, from Princeton University, Princeton, NJ, USA, in 1989. Since then, he has been with the University of Notre Dame, Notre Dame, IN, USA, currently holding the position of Associate Professor with the Department of Electrical Engineering. His research has been funded by GE Health Care, NASA, the National Science Foundation, Electricite de France, the Department of Homeland Security and the State of Indiana's 21st Century Fund. His research interests include primarily within the domain of inverse problems, with particular concentration in tomography for medical diagnostic imaging and nondestructive evaluation, stochastic image modeling for Bayesian estimation, numerical methods for optimization, and general nonlinear estimation techniques.